Key Points:
- We observed the traveling ionospheric disturbances (TIDs) at the low latitudes
- We used the simultaneous observations by 630.0-nm airglow imager and the CHAMP satellite
- We concluded the TIDs caused by the gravity waves in the neutral atmosphere

Supporting Information:
- Supporting Information S1
- Movie S1
- Movie S2
- Movie S3

Correspondence to:
A. Ceren Moral,
acmoral@isee.nagoya-u.ac.jp

Citation:
Moral, A. C., Shiokawa, K., Suzuki, S., Liu, H., Otsuka, Y., & Yatini, C. Y. (2019). Observations of low-latitude traveling ionospheric disturbances by a 630.0-nm airglow imager and the CHAMP satellite over Indonesia. *Journal of Geophysical Research: Space Physics*, *124*, 2198–2212. https://doi.org/10.1029/2018JA025634

Observations of Low-Latitude Traveling Ionospheric Disturbances by a 630.0-nm Airglow Imager and the CHAMP Satellite Over Indonesia

Aysegul Ceren Moral[1] [ID]**, Kazuo Shiokawa[1]** [ID]**, Shin Suzuki[2], Huixin Liu[3]** [ID]**, Yuichi Otsuka[1]** [ID]**, and Clara Yoko Yatini[4]**

[1]Institute for Space-Earth Enviromental Research, Nagoya University, Nagoya, Japan, [2]Faculty of Regional Policy, Aichi University, Toyohashi, Japan, [3]Deparment of Earth and Planetary Science, Faculty of Science, Kyushu University, Fukuoka, Japan, [4]Space Science Center, the Indonesian National Institute of Aeronautics and Space (LAPAN), Bandung, Indonesia

Abstract We report the first comparison of ground and satellite measurements of low-latitude traveling ionospheric disturbances (TIDs). Three TID events were simultaneously observed by a 630.0-nm airglow imager and the CHAllenging Minisatellite Payload (CHAMP) satellite at Kototabang, Indonesia (geographic coordinates: 0.2° S, 100.3° E, geomagnetic latitude: 10.6° S). In 630.0-nm airglow images of all three events, there are clear southward-moving structures. Events 1 and 2 are a single pulse with horizontal scales of ~500–1,000 km. Event 3 shows five wave fronts with a horizontal scale size of 500–1,000 km. All three TIDs are medium-scale TIDs. Horizontal wavelengths of both airglow intensity at an average emission altitude of 250 km and CHAMP neutral density variations measured at 400 km are estimated by fitting a sinusoidal function to the observed data. The estimated horizontal wavelengths for airglow and neutral density data are 1,031 and 880 km for event 1 and 560 and 420 km for event 3, respectively. These values between airglow and CHAMP are comparable, suggesting both instruments are observing the same wave. For event 1, the CHAMP electron density mapped along the geomagnetic field line onto the airglow altitude does not show wave structure similar to the airglow variation. For events 2 and 3, the plasma density did not show wavy structures similar to the waves seen in the airglow image and CHAMP neutral density. These results suggest that the TIDs observed in airglow images are not caused by ionospheric plasma instability but by gravity waves in the thermosphere.

1. Introduction

Traveling ionospheric disturbances (TIDs) are wave-like features in the ionosphere. Those with a typical scale between 100 and 1,000 km and those larger than 1,000 km are referred to as medium-scale TIDs (MSTIDs) and large-scale TIDs (LSTIDs), respectively (Hunsucker, 1982). TIDs are widely studied by using ground-based instruments, such as airglow imagers (e.g., Mendillo et al., 1997; Shiokawa et al., 2003), ionosondes (e.g., Bowman, 1990), radar (e.g., Fukao et al., 1991; Waldock & Jones, 1986), and multipoint GPS receivers (e.g., Kotake et al., 2014). However, the source of these disturbances is not yet understood. There are two main proposals for the source of TIDs: gravity waves in the thermosphere and plasma instabilities in the ionosphere. Hines (1960) suggested that gravity waves are the source of observed TIDs, and many studies support that suggestion (e.g., Hunsucker, 1982). However, there are also many studies that suggest that the ionospheric Perkins instability might be the cause of the TIDs (Kotake et al., 2014; Miller et al., 1997; Shiokawa et al., 2003).

Imagers of 630.0-nm airglow emissions have been used to observe ionospheric variations. The altitude of the 630.0-nm airglow emission layer is considered to be 200–300 km. At that altitude, the dominant chemical reaction for airglow emission is $O^+ + O_2 \rightarrow O_2^+ + O$, which means that airglow emissions are dependent on the density variations of molecular oxygen, O_2, and oxygen ions, O^+. The density of O_2 decreases exponentially with increasing altitude where O^+ is the main ion source in the ionosphere and its density follows the Chapman distribution. If the height of the F layer (O^+ layer) decreases, this leads to increased interaction between O^+ and O_2, causing an increase in the 630.0-nm airglow emission as explained by many studies (e.g., Mendillo & Baumgardner, 1982; Sobral et al., 1985; Torr & Torr, 1982).
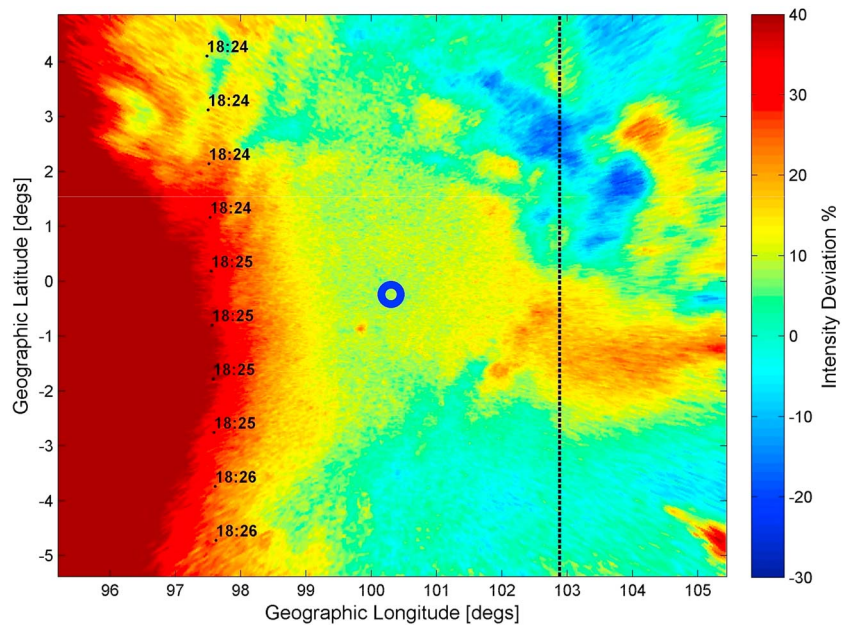
Figure 1. This airglow image in geographical coordinates is the deviation from 1-hr running averages at the time when CHAllenging Minisatellite Payload was over Kototabang at ~18:26 UT (01:26 LT) on 30 April 2006. The color scale on the right side of the figure shows the values of the deviation in percent. The dashed line indicates the line where we obtain the keogram shown in Figure 2b.

The Perkins instability (Perkins, 1973) in the *F* region of the ionosphere is one of the mechanisms that causes ionospheric variability. Otsuka et al. (2013) showed that at midlatitudes, nighttime MSTIDs have a dominant southwestward propagation in the northern hemisphere. They suggested that the electrodynamics of the ionosphere is the reason behind the generation of nighttime MSTIDs. Yokoyama et al. (2009) simulated MSTIDs using a three-dimensional numerical model and showed that the sporadic *E* layer, E_s, contributes to the Perkins instability and amplifies the perturbation.

Kotake et al. (2014) used total electron content data obtained by multipoint GPS receivers and showed that midlatitude daytime MSTIDs mostly propagate in a southeastward direction in the northern hemisphere and are likely to be generated by gravity waves. Midlatitude nighttime LSTIDs caused by gravity waves were studied by Tsugawa et al. (2004) using GPS-total electron content (TEC) observations. They found a clear correlation between geomagnetic activity and the occurrence rate of LSTIDs.

At equatorial latitudes, Shiokawa et al. (2006) studied nighttime MSTIDs using 2 years of data of 630.0-nm airglow observations at Kototabang (KTB), Indonesia. They found quasiperiodic southward-moving waves and suggested that gravity waves in the thermosphere are the source of the observed waves. Fukushima et al. (2012) studied the 7-year statistical characteristics of nighttime MSTIDs observed in the 630.0-nm airglow images over KTB. They examined the dependence of the occurrence rate and horizontal wavelength of MSTIDs on solar activity. They found that the dominant propagation direction of the observed MSTIDs over KTB was southward. They interpreted their results as showing that gravity waves caused the MSTIDs and they suggested that deep convection in the troposphere generates the gravity waves that are the source of their events.

From a simulation of gravity wave propagation in the thermosphere, Vadas (2007) suggested that propagation to higher altitudes in the thermosphere is not possible for gravity waves with horizontal wavelengths smaller than 400 km due to the dissipation of the gravity waves in the thermosphere. She also pointed out that gravity waves with a phase speed greater than the speed of sound cannot exist in the lower atmosphere (less than 300-km altitude), thus the thermosphere may be the source of the secondary waves generated at higher altitudes from the dissipation of primary waves originating at lower altitudes. Recent studies support the idea that gravity waves created in the lower atmosphere can propagate to the upper atmosphere and become the source of TIDs (e.g., Oberheide et al., 2015). Fukushima et al. (2012) compared the horizontal propagation directions of MSTIDs and the locations of tropospheric convection, identified by equivalent
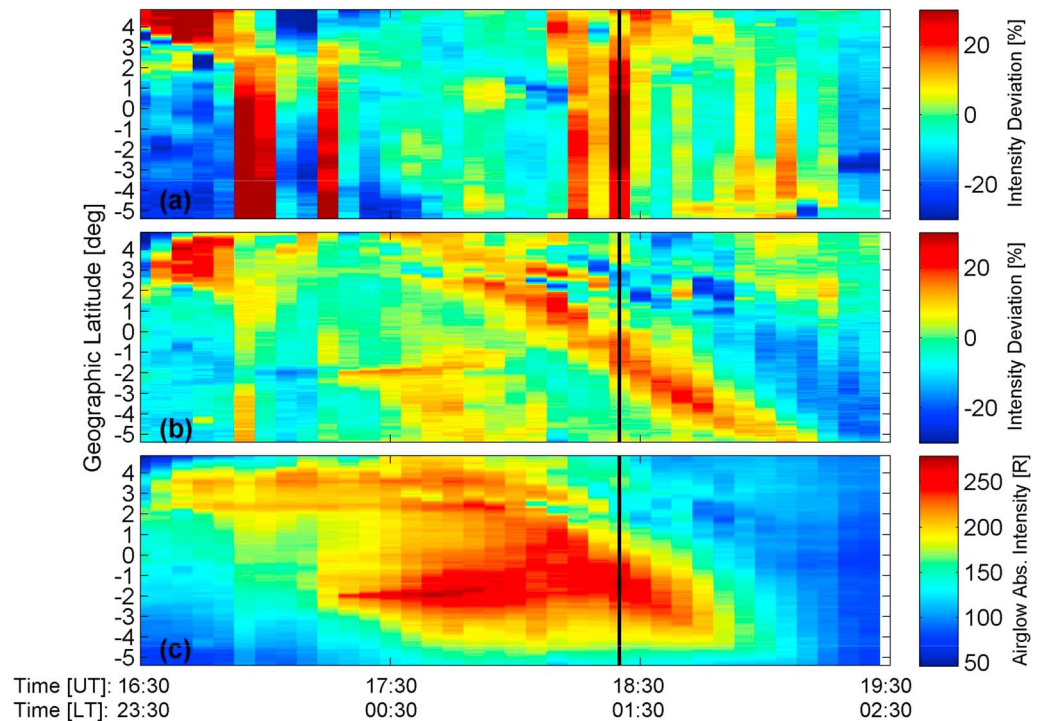
Figure 2. Meridional keograms of the 630.0-nm airglow images observed on 30 April 2006 from 16:30 to 19:30 UT. (a) Keogram contaminated by the artificial light in deviations from 1-hr running averages along the trajectory of the CHAllenging Minisatellite Payload satellite (~ longitude 98.5° E). (b) Keogram in deviations from 1-hr running averages along the longitude of 102.86° shown by a vertical dashed line in Figure 1. (c) Keogram with absolute intensities in Rayleigh along the same baseline as that of Figure 2b. LT = local time.

black body temperature, and suggested that 81% of the MSTIDs at KTB are generated from deep convection in the troposphere.

A statistical study of thermospheric mass density measured by the CHAllenging Minisatellite Payload (CHAMP) satellite by Liu et al. (2005) during both quiet and disturbed conditions at low and midlatitudes showed that mass density increases with increased geomagnetic activity but the main structure stays similar. Low-latitude thermospheric density and its local time (LT) and seasonal variations were studied by Müller et al. (2009). They examined 4 years of data from the CHAMP satellite and found that density peaks occurred during equinoxes and the lowest density occurred around the June solstice. Park et al. (2014) studied mid-latitude and low-latitude thermospheric gravity waves by using CHAMP mass density measurements taken during daytime hours (09–18 hr LT). They found that gravity wave activity is stronger during a solar minimum, which is consistent with stratospheric gravity wave characteristics. They concluded that the main source of the gravity waves observed by CHAMP is in the troposphere or stratosphere. Previous research mentioned above uses only CHAMP observation data; the novelty of our research is that we use 2-D airglow images and combine them with in situ CHAMP measurements to obtain a better understanding of the nature of the gravity waves and their propagation in the upper atmosphere. In this study, we compared simultaneous observations of three equatorial TID events made by a ground-based 630.0-nm airglow imager and the CHAMP satellite to determine the sources of the equatorial TIDs. We compared airglow variations during those waves with the neutral and electron densities measured by the CHAMP satellite.

2. Observations

The TIDs reported in this paper were observed by an airglow imager installed at the KTB station, Indonesia (geographic coordinates: 0.2° S, 100.3° E, geomagnetic latitude: 10.6° S, LT: universal time [UT] + 7 hr). Airglow images at a 630.0-nm wavelength (OI), with an assumed emission altitude between 200 and 300 km, are taken every 4.5 min with an exposure time of 105 s. Background emissions at a wavelength of 572.5 nm are obtained every 30 min. TIDs in these airglow images have been recorded for a 7-year period from
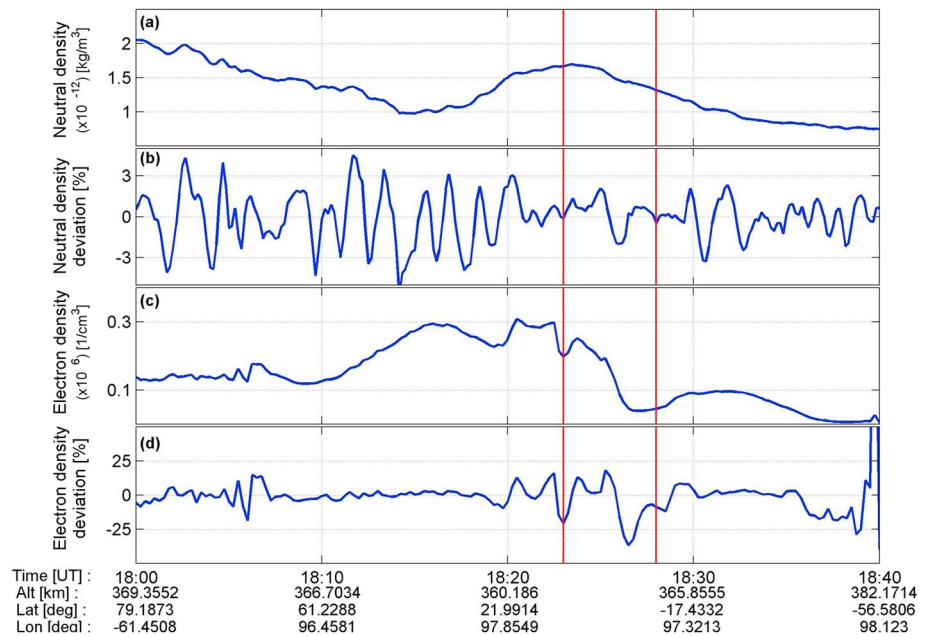
Figure 3. Neutral and electron densities and their deviations observed by the CHAllenging Minisatellite Payload satellite during event 1: (a) neutral density, (b) neutral density deviation, (c) electron density, and (d) electron density deviation. Deviations are obtained by subtracting 2-min running averages from the original data, corresponding to the horizontal distance of 1,000 km covered by the satellite's motion. The time interval between the two vertical red lines indicates the time when the satellite was in the field-of-view of Kototabang.

October 2002 to October 2009 (Fukushima et al., 2012). We selected TID events for which the CHAMP satellite trajectory was within 500 km of KTB where 500 km is taken because it is the half of the distance of the field-of-view of airglow observations. As a result, only three potential simultaneous ground-satellite measurement events were obtained from the 7-year data set. The dates of these events were 30 April 2006 (event 1), 28 September 2006 (event 2), and 12 April 2004 (event 3). The tropical weather conditions of Indonesia where the probability of clear sky is less than 10% for most of the year, as reported by Shiokawa et al. (2006), is the main reason why we have only a few suitable dates in 7 years of data.

The CHAMP satellite was launched in July 2000 and reentered the atmosphere in September 2010. Initially, the altitude of the satellite was 450 km (for our events, the average altitude of the CHAMP satellite was around 400 km) and decayed over the years. CHAMP had a near-circular orbit (Reigber et al., 2002). In this study, we used neutral and electron density observations of the CHAMP satellite. Instruments on the satellite are described in the paper by Lühr et al. (2012). Electron density and electron temperature are measured by the planar Langmuir probe on the satellite. An accelerometer is located at the center of gravity of the satellite to sense only the nongravitational force on the satellite. Thermospheric mass density and wind are deduced from the air drag experienced by the satellite.

TIDs are not easy to distinguish in raw airglow images. To identify the wave structures clearly, we converted raw all-sky airglow images to geographical coordinates with the assumption that the airglow layer is located at an altitude of 250 km. The raw and converted images consists of 512×512 pixels. After the coordinate conversion, we subtracted 1-hr (± 30 min from every image) running averages I_a from the center image I of that 1-hr period. Then, we divided the subtracted image by the 1-hr average to obtain the percentage value I_d, which is called the percentage deviation image ($I_d = 100 \times (I - I_a)/I_a$). After constructing the percentage deviation images, we defined the criteria to identify TIDs as moving perturbations in consecutive images even if it is only a one pulse.

In this paper, we examine in detail the three simultaneous ground-satellite measurement TID events.

2.1. Event 1: 30 April 2006

Event 1 was observed on 30 April 2006. Figure 1 shows an airglow image in geographical coordinates as a deviation from 1-hr running averages at the time when CHAMP was over KTB at 18:26 UT (01:26 LT). Black dots with corresponding time stamps are indicators of the CHAMP satellite trajectory.
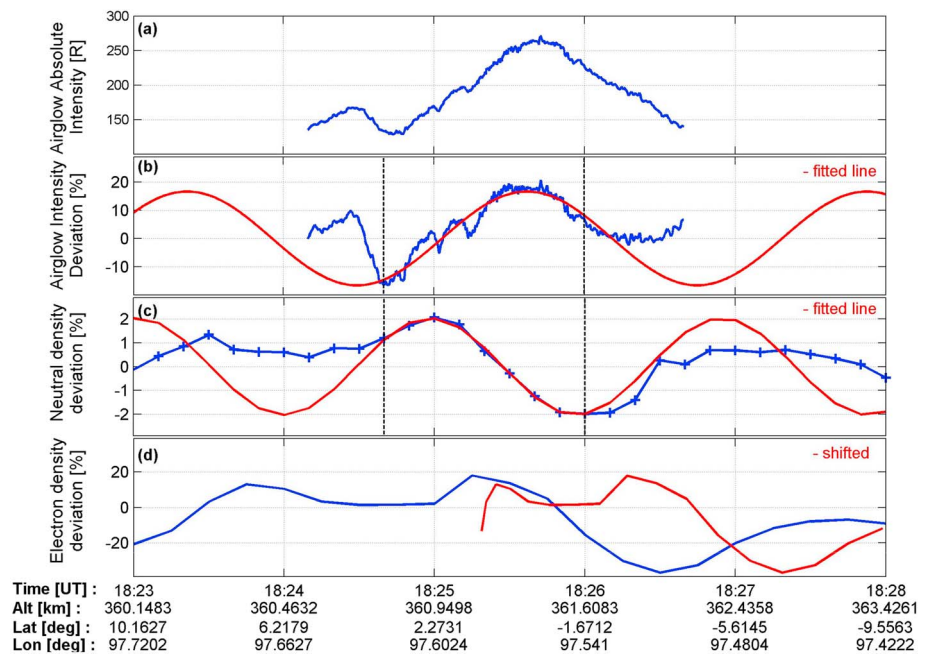
Figure 4. Airglow intensity variations and the CHAllenging Minisatellite Payload satellite neutral and electron-density deviations: (a) absolute intensity in Rayleigh and (b) percentage deviation of airglow intensity observed by the 630.0-nm airglow imager, along the black solid line in Figures 2c and 2b; (c) neutral-density deviation and (d) electron density deviation measured by CHAllenging Minisatellite Payload from 18:23 to 18:28 UT. Red lines in (b) and (c) show the results of sinusoidal fitting to the data range between the dashed black lines of that panel, and the red line in (d) is the electron density deviation shifted along the geomagnetic field line from the satellite altitude to the assumed airglow altitude of 250 km by using the IGRF geomagnetic field model. The altitude, geographic latitude, and longitude of the satellite are shown at the bottom of the figure.

The circle at the center of the figure shows the location of the KTB station. CHAMP is moving from the northern to southern hemisphere during this event. The intense emission in the left side of the image is contamination from an artificial light near the observatory hut. An east-west aligned enhancement in the airglow emission due to the wave can be observed at latitudes between $\pm 3°$.

Movie S1 in the supporting information shows the sequential airglow images from 16:30 to 19:30 UT in the same format as that of Figure 1. A clear southward movement (as the KTB station is geomagnetically in the southern hemisphere, southward movement means poleward movement) of the TID can be seen from 17:31 to 19:15 UT in this movie.

In order to estimate horizontal wavelengths and phase velocities of the observed TIDs, we made meridional keograms. We took a meridional pixel strip (11×512 pixels) of percentage deviation image shown in Figure 1 along the CHAMP satellite trajectory and took longitudinal 11 pixels ($0.21°$ in longitude) averages for every image and stacked them together in one plot in the order of their time stamps.

Figure 2 shows the meridional keograms of the event from 16:30 to 19:30 UT. A keogram is a figure of multiple airglow images stacked in one figure over constant latitude or longitude. Due to the contamination of an artificial light source in the west side of the airglow images along the CHAMP trajectory in Figure 1, three keograms are prepared for this event. Figure 2a shows the keogram along the exact trajectory of the satellite, which is completely in the contaminated part of the airglow image. We observe a wave passage with an east-west alignment in the Figure 1 and Movie S1, so Figure 2b shows a keogram along the longitude of $102.86°$ (shown by the vertical dashed line in Figure 1) to avoid the effects of the light contamination observed along the CHAMP longitude.

Figures 2a and 2b are keograms showing the deviation in percent from 1-hr running averages. Figure 2c is a meridional keogram with the absolute intensities in Rayleigh along the same baseline as Figure 2b. Black lines in the figure mark the time ($\sim$18:26 UT) when the CHAMP satellite crossed over KTB. Figure 2a is highly contaminated by the flickering artificial light. On the other hand, Figure 2b shows a clear wave
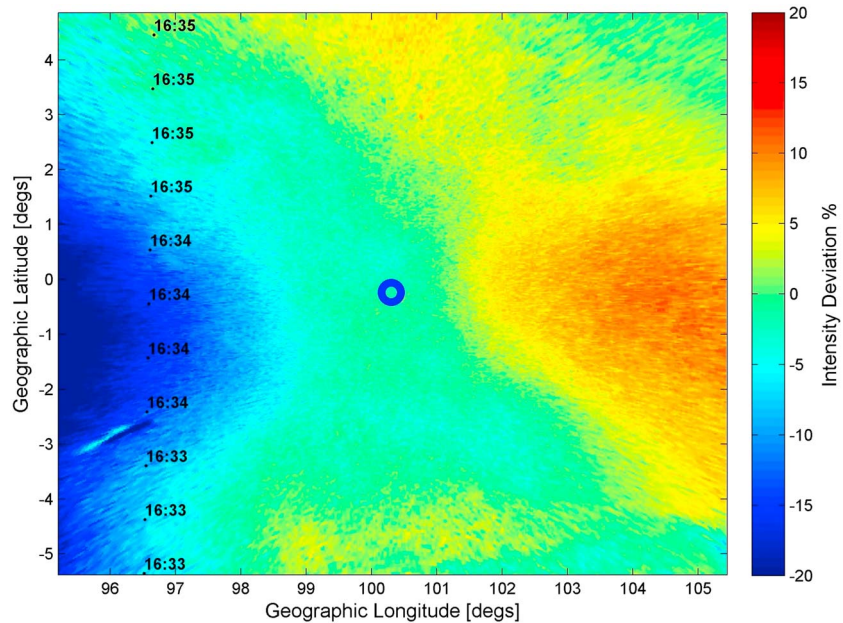
Figure 5. Airglow image in geographical coordinates showing deviations from 1-hr running averages when CHAllenging Minisatellite Payload was over Kototabang at 16:33 UT (23:33 LT) on 28 September 2006. The color scale on the right side of the figure shows the values of the deviation in percent.

front with a north-south scale of approximately 700 km from 17:30 to 18:45 UT, where the intensification of airglow is greater than 250 R at 18:20 UT in Figure 2c. From this keogram, we estimated the southward velocity of the wave to be approximately 112 m/s by fitting a straight line on the keogram. The ambiguities of the velocity would be less than ±20 m/s for this case.

Neutral and electron densities and their deviations observed by the CHAMP satellite during event 1 are shown in Figure 3. Red lines in the figure indicate the CHAMP satellite location and time within a 500-km radius from KTB. Time, altitude, latitude, and longitude values are shown below the figure. Both neutral density and electron density values are decreasing near KTB, as shown in Figures 3a and 3c. The electron-density deviation in Figure 3d shows variations for the whole passage. However, the intensity of those variations increases near KTB, while the neutral-density deviation in Figure 3b is fluctuating throughout the plotted satellite pass with amplitudes of a few percent.
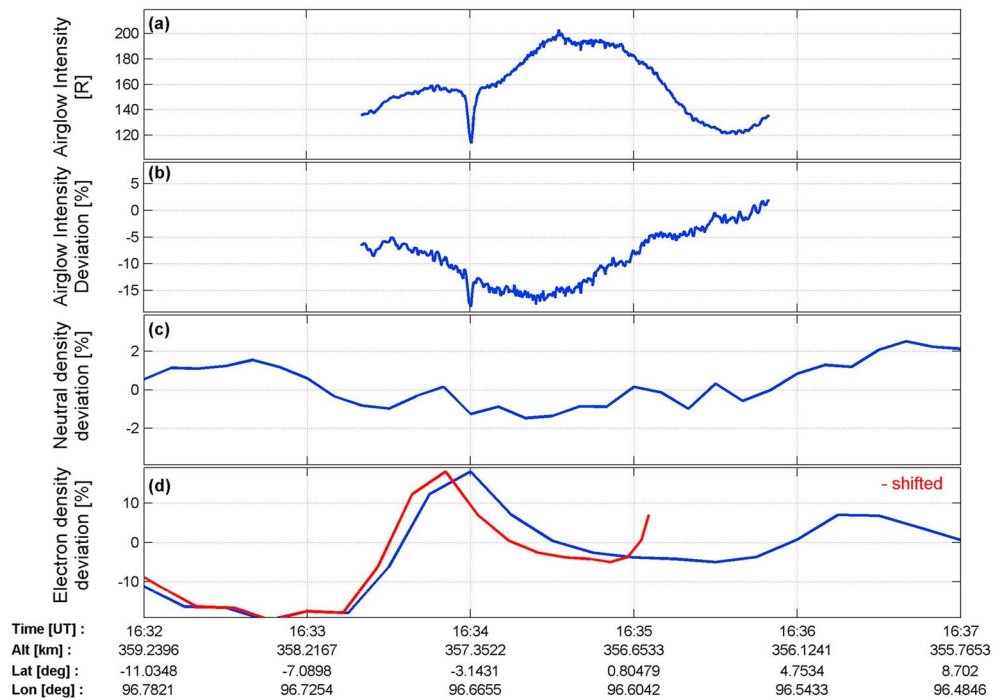
Figure 4 compares airglow image variations and the CHAMP satellite neutral and electron-density deviations. We fitted a sinusoidal function to obtain frequencies and the phase difference between airglow and neutral density variations. We used the sinusoidal function $A \sin(kx + \phi)$, where A, k, and ϕ represent the amplitude, wave number, and phase for the data set. The red lines in Figure 4b and 4c are the fitted lines for the data range indicated by the two black dashed lines, which are selected visually by choosing the data from the enhancement observed in the airglow images, in the graphs of airglow intensity and neutral density deviations. We extended the plot of the fitted sinusoidal function to the whole passage to see the wave components clearly. The red line in the Figure 4d is the electron density deviation shifted along the geomagnetic field line from the satellite altitude, ~380 km for this event, to the assumed airglow altitude, 250 km, by using the International Geomagnetic Reference Field (IGRF) model. Figures 4a and 4b show a clear enhancement of the airglow intensity with a peak at a geographic latitude of −1°, corresponding to the southward-moving wave (which can be clearly seen in Figure 2). Both neutral density deviation in Figure 4c and electron density deviation in Figure 4d (blue line) shows similar wave features throughout the plotted interval. The amplitude of neutral density variations, shown in Figure 4c, are 1–2%. Electron density deviations, shown as blue line in Figure 4d, follows the airglow enhancement observed in Figure 4b. However, electron density variations mapped on the airglow layer along the magnetic fields, red line on Figure 4d, do not show wave structure similar to the airglow enhancement. In the Figure 4d, the electron density has more than 20% variation. For event 1, the frequency components calculated by the sinusoidal fitting are 0.00609 and 0.00714 rad/km for airglow intensity deviation and neutral-density deviation, corresponding
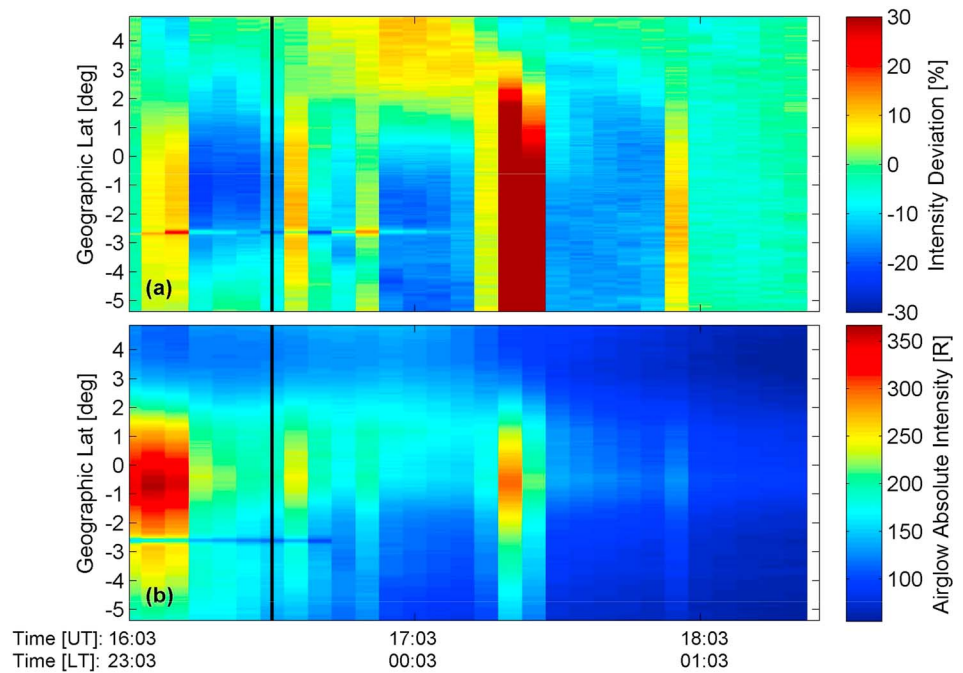
Figure 6. Meridional keograms of the 630.0-nm airglow images observed on 28 September 2006 from 16:03 to 18:33 UT. (a) Keogram of deviations from 1-hr running averages along the trajectory of the CHAllenging Minisatellite Payload satellite (longitude 96.5° E). (b) Keogram with the absolute intensities in Rayleigh. Black lines mark the time (16:33 UT) when the CHAllenging Minisatellite Payload satellite crossed over Kototabang. LT = local time.
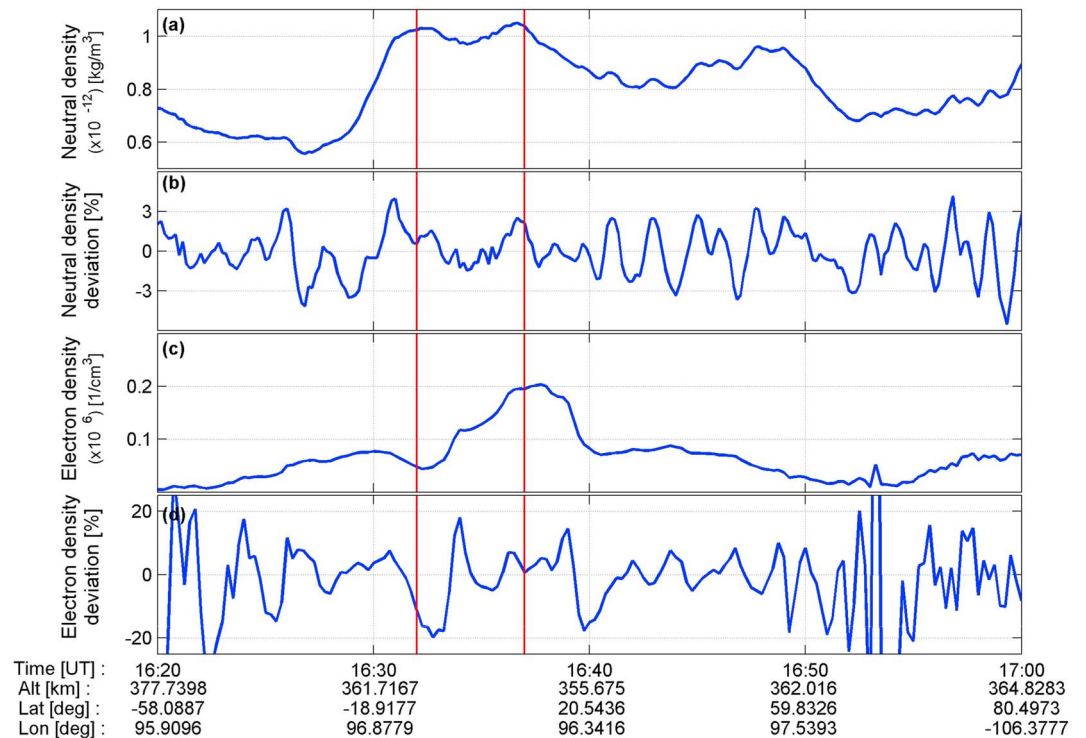
Figure 7. Neutral and electron densities and their deviations observed by the CHAllenging Minisatellite Payload satellite during event 2: (a) neutral density, (b) neutral density deviation, (c) electron density, and (d) electron-density deviation. Deviations are obtained by subtracting 2-min running averages from the original data, corresponding to the horizontal distance of 1,000 km covered by the satellite's motion. The time interval shown by two vertical red lines indicates when the satellite was in the field-of-view of Kototabang.

Time [UT] :	16:32	16:33	16:34	16:35	16:36	16:37
Alt [km] :	359.2396	358.2167	357.3522	356.6533	356.1241	355.7653
Lat [deg] :	-11.0348	-7.0898	-3.1431	0.80479	4.7534	8.702
Lon [deg] :	96.7821	96.7254	96.6655	96.6042	96.5433	96.4846

Figure 8. Airglow intensity variations and the CHAllenging Minisatellite Payload satellite neutral and electron-density deviations: (a) absolute intensity in Rayleigh and (b) percentage deviation of airglow intensity, observed by 630.0-nm airglow imager; (c) neutral-density deviation and (d) electron density deviation measured by the CHAllenging Minisatellite Payload from 16:32 to 16:37 UT. The red line in (d) is the electron density deviation shifted along the geomagnetic field line from the satellite altitude to the assumed airglow altitude of 250 km by using the IGRF geomagnetic field model. The altitude, geographic latitude, and longitude of the satellite are shown at the bottom of the figure.

to horizontal wavelength of approximately 1,031 and 880 km, respectively. The calculated phase difference between airglow data and neutral density is 63°. We consider that these two wavelengths are comparable, indicating that both the airglow imager and CHAMP are observing the same wave in the thermosphere.

2.2. Event 2: 28 September 2006

Figure 5 shows the 630.0-nm airglow image when the CHAMP satellite passed over KTB at 16:33 UT (23:33 LT) on 28 September 2006 in the same format as in Figure 1. The CHAMP satellite trajectory is shown by black dots, and the time stamp of the passage is shown next to the dots. On the bottom left part of the figure, between −2 and −3 geographic latitude and 96–97 geographic longitude degrees, a small light contamination by a bright star can be seen. This contamination is not affecting the wave passage. Same contamination can be seen in bottom left part of Figures 6a and 6b. The satellite was moving from the southern to the northern hemisphere for this event. A TID causes the enhancement of airglow at the northward edge above ∼3°N in the figure. Movie S2 shows the sequential airglow images from 16:03 to 18:33 UT. The south-ward movement of a TID can be seen at 16:16–17:23 UT, though the structure did not reach the zenith of the image.

Meridional keograms of event 2 are shown in Figure 6 in the same layout as Figure 2. Figures 6a and 6b show the keogram along the CHAMP satellite trajectory (∼longitude 96.5° E) for percentage deviations and absolute intensity, respectively. A wave front with a scale of approximately 500 km moving southward with a velocity of 124 m/s can be observed from 16:15 to 17:30 UT at latitudes higher than 1° N in Figure 6a. As with event 1, this event is only a single pulse of 630.0-nm airglow intensification moving southward (geomagnetically poleward) at 24 LT.

Figure 7 shows the neutral and electron densities and their deviations measured by the CHAMP satel-lite in the same format as Figure 3. The neutral density in Figure 7a is first decreasing then increasing when the CHAMP satellite passes close to KTB (the times between the red lines), while the electron density in Figure 7c is increasing, probably toward the equatorial anomaly. Both the neutral density
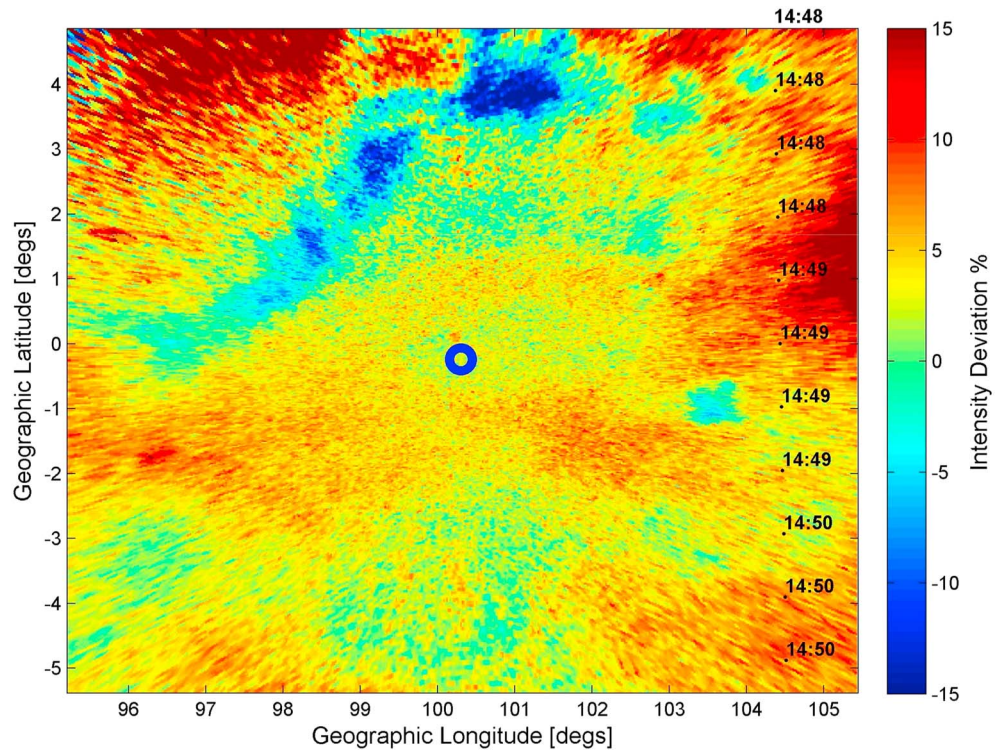
Figure 9. Airglow image in geographical coordinates of deviations from 1-hr running averages when CHAllenging Minisatellite Payload was over Kototabang at 14:49 UT (21:49 LT) on 12 April 2004. The color scale on the right side of the figure shows the values of the deviation in percent.
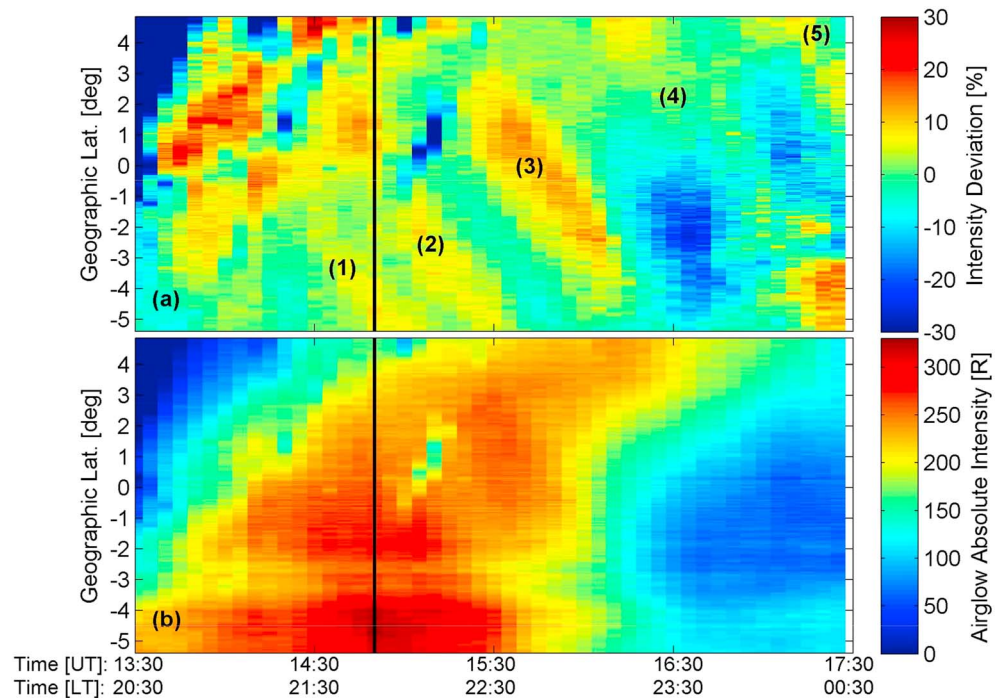
Figure 10. Meridional keograms of the 630.0-nm airglow images observed on 12 April 2004 from 13:30 to 17:30 UT. (a) Keogram of deviations from 1-hr running averages along the trajectory of the CHAllenging Minisatellite Payload satellite (longitude 104.5° E). (b) Keogram with the absolute intensities in Rayleigh. Black lines mark the time (14:51 UT) when the CHAllenging Minisatellite Payload satellite crossed over Kototabang. Observed wave fronts are marked with numbers 1 to 5 in (a). LT = local time.
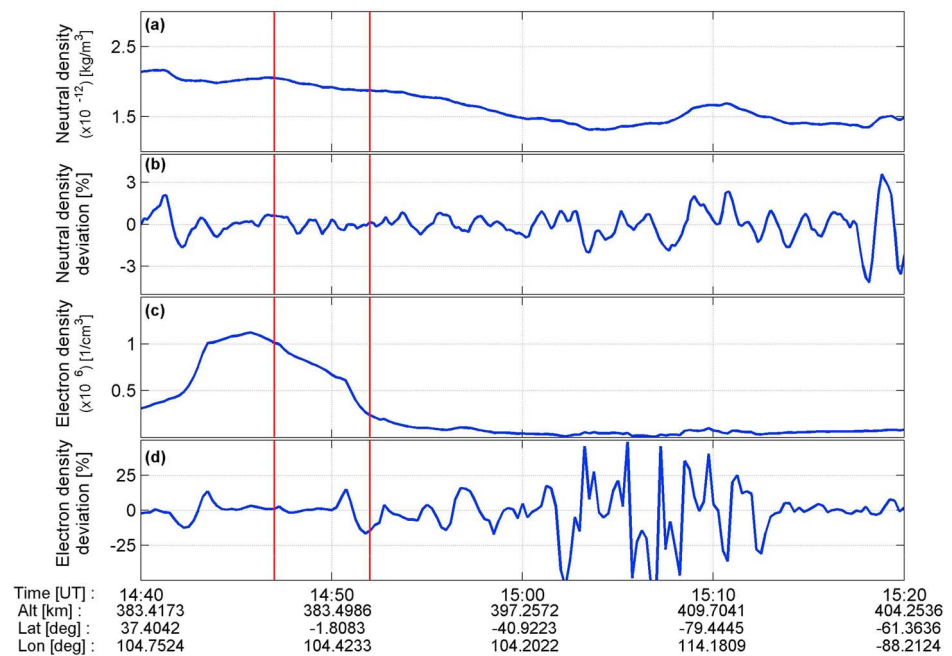
Figure 11. Neutral and electron densities and their deviations observed by the CHAllenging Minisatellite Payload satellite during Event 3: (a) neutral density, (b) neutral-density deviation, (c) electron density, and (d) electron density deviation. Deviations are obtained by subtracting 2-min running averages from the original data, corresponding to the horizontal distance of 1,000 km covered by the satellite's motion. The time interval shown by two vertical red lines indicates when the satellite was in the field-of-view of Kototabang.
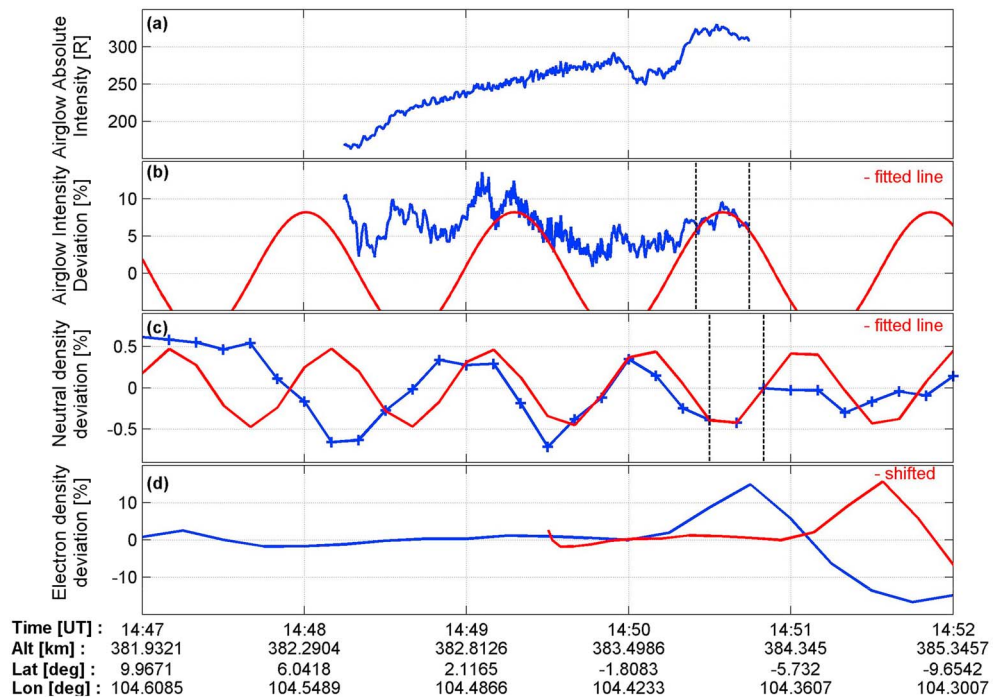
and electron-density deviations in Figures 7b and 7d show some fluctuations throughout the pass with amplitudes less than 1% and about 20%, respectively.

Figure 8 shows the comparison of airglow image variations and the CHAMP satellite neutral and electron-density deviations. A small contamination of the airglow images creates the dip at −3.14°N in Figures 8a and 8b. CHAMP satellite passed KTB before the southward-moving MSTID appeared over KTB, so that MSTID signature is seen only at the northern edge of the airglow data. At the northern end (right side), the airglow intensity increases with latitude (Figure 8b). From the airglow intensity variations shown in Figure 8b, horizontal wavelength cannot be determined. Figures 8c and 8d are the neutral and electron-density deviations measured by CHAMP from 16:32 to 16:37 UT. The neutral-density deviation in Figure 8c does not shows oscillation which could be caused by gravity waves but increases with latitudes in the same way as the airglow intensity variation at geographic latitudes of 1–4°N with an amplitude less than 1%. The relationship of airglow variation with electron density deviations is unclear for this case.

2.3. Event 3: 12 April 2004

The third event was observed on 12 April 2004. Figure 9 (layout same as Figure 1) shows the 630.0-nm airglow image at the conjunction time of 14:49 UT (21:49 LT) when the CHAMP satellite passed over KTB. The satellite is moving from the northern to the southern hemisphere for this event. An MSTID structure can be seen between +1° and −2° latitudes with an east-west aligned front. Movie S3 was made to show the sequence of the whole event from 13:30 to 17:30 as deviations from 1-hr running averages. Clear southward-moving structures can be repeatedly seen in this movie during the period 14:30–17:30 UT. It should be noted that we did not examine the westward-moving structures that can be seen before the event time (before 14:30 UT) in Movie S3.

Figure 10 shows the meridional keograms for this event in the same format as that of Figure 2. Five clear wave fronts (numbered (1) to (5)) moving southward can be seen in Figure 10a in the period 14:30–17:30 UT, unlike events 1 and 2, which were single pulses. Horizontal wavelengths between the consecutive wave fronts are 500, 700, 1,000, and 900 km. These wave fronts are moving southward with a velocity of approximately 280 ± 20 m/s. In Figure 10b, there is an intensification in the absolute intensity with a northward movement, which could be due to the equatorial ionization anomaly. The intensification of airglow is greater than 250 R at 14:40 UT in Figure 10b.

Figure 12. Airglow intensity variations and the CHAllenging Minisatellite Payload satellite neutral and electron-density deviations: (a) absolute intensity in Rayleigh and (b) percentage deviation of airglow intensity, observed by 630.0-nm airglow imager; (c) neutral-density deviation and (d) electron-density deviation measured by CHAMP from 14:47 to 14:52 UT. Red lines in (b) and (c) show the results of sinusoidal fitting to the data range between the dashed black lines of that panel, and the red line in (d) is the electron density deviation shifted along the geomagnetic field line from the satellite altitude to the assumed airglow altitude of 250 km by using the IGRF geomagnetic field model. The altitude, geographic latitude, and longitude of the satellite are shown in the bottom of the figure.

Neutral and electron densities and their deviations are shown in Figure 11 in the same format as in Figure 3. The neutral density shown in Figure 11a is decreasing during the event. In Figure 11c, KTB is located on the equatorward edge of the electron density enhancement which probably corresponds to the equatorial anomaly. Both the neutral-density deviations in Figure 11b and electron-density deviations in Figure 11d are fluctuating throughout the passage of the satellite over KTB with amplitudes of 0.5–1% and 10%, respectively.

Figure 12 shows a comparison of the airglow intensity and the CHAMP satellite density deviations in the same format as that in Figure 4. The enhancement caused by the wave front in the airglow keogram can be seen at the southern edge (right side) of Figures 12a and 12b. The neutral-density deviation in Figure 12c shows quasiperiodic wave-like oscillations throughout the event with an amplitude of 1%. This neutral-density deviation has an out-of-phase relationship with the airglow wave enhancement in Figures 12a and 12b. However, the electron density deviations in Figure 12d do not show clear a correspondence to the waves in the airglow and neutral-density deviations. We applied the sinusoidal fitting for event 3, in the same way as for event 1, for the ranges shown by vertical dashed lines in Figures 12b and 12c. Due to different spatial resolution differences of CHAMP satellite and airglow image data, we could not use the same fitting range for Figures 12b and 12c. From the fitting, we obtained similar frequency components of 0.01123 and 0.01504 rad/km, corresponding to horizontal wavelengths of approximately 560 and 420 km, for the airglow intensity and neutral-density deviations, respectively. The estimated horizontal wavelength of the observed MSTID from the Figure 10a is ≈500 km, which is consistent with the estimated horizontal wavelength of the fitting. This shows us that the selected fitting range for the airglow is valid for this event. This fitting gives us a phase difference of 190° between the airglow intensity and the neutral density deviation.

3. Discussion

We have presented three ground-satellite conjugate measurements of TIDs at an equatorial station, KTB. All three events were southward-moving structures in 630.0-nm airglow images. We applied the nonlinear least

squares method to fit a sinusoidal function to both airglow intensity deviation and neutral-density deviation to show wave numbers. Calculated results are highly sensitive to the data range given as an input to the fitting. We marked the input data for the fitting with dashed lines in Figures 4b and 4c (event 1) and 12 (event 3). We looked the horizontal wavelengths obtained from the fittings to understand if both measurements are of the same wave or not. For events 1 and 3, we calculated the wave lengths of airglow intensity and neutral-density variations as 1,031 and 880 km and 560 and 420 km, respectively. Horizontal wavelengths of the airglow and neutral density deviations are comparable. In the case of gravity waves, perturbations we observe from the airglow emission should show similar wave features with the neutral density perturbations observed by the CHAMP. Thus, we think that gravity waves in the neutral atmosphere are likely to be the source of the observed TIDs in events 1 and 3. In event 2, although southward-propagating MSTIDs were observed in the 630.0-nm airglow images, the corresponding neutral density deviations were not observed by the CHAMP in situ measurement.

From the comparison between the electron density and airglow intensity in the same geomagnetic field line, corresponding wave structure is not clear for all of the events. This lack of correspondence indicates that the observed TIDs are not generated as a result of plasma instability in the ionosphere in the following reason. If TIDs are caused by a plasma instability, polarization electric fields generated by the plasma instability are transmitted along the geomagnetic fields without attenuation and move the plasma by ExB drifts in the direction perpendicular to the magnetic fields causing the plasma density modulation at the altitude of the CHAMP satellite. However, such plasma density modulations were not observed in the electron density data obtained by the CHAMP satellite.

Both neutral and electron densities observed with the CHAMP satellite in situ measurements show similar wave features and horizontal wavelengths for event 1; however, similar features are not observed in events 2 and 3. This could be because of the difference of amplitudes of the neutral wind variation. For event 1, peak-to-peak amplitude was approximately 4%, and for events 2 and 3, amplitudes were less than 1%. Gravity waves with small amplitude of neutral wind variations in events 2 and 3 could not cause discernible plasma density variations.

It is generally expected to observe similar wave structures between electron density and the airglow variations caused by atmospheric gravity waves. Wave fluctuations in both neutral density and wind can cause plasma fluctuations in the same frequency. According to Hooke (1968), the phase relationship between plasma density and neutral density variations depends on wave parameters. Because plasma can move only along the magnetic field lines, when poleward (equatorward) neutral wind forces neutrals and plasma to move, plasma can only move downward (upward) along the magnetic field line. Since the CHAMP satellite is located at altitudes higher than the peak of the F region, a poleward neutral wind (pushing plasma down) causes a decrease of the electron density. Gravity waves also cause convergence and divergence of the plasma along the magnetic field line. Phase relationship between plasma density and neutral density variations depends on balance of these two effects.

Gravity waves in the neutral atmosphere cause density and wind velocity oscillations at the same frequency and same spatial scale. If gravity waves are the source of the observed TIDs, then the following linear dispersion relationship must be satisfied by the observed TIDs (Hines, 1960):

$$m^2 = \frac{N^2}{(u-c)^2} - k^2 - \frac{1}{4H^2}, \tag{1}$$

where the vertical and horizontal wave numbers are represented as $m\,(=\,2\pi/\lambda_z)$ and $k\,(=\,2\pi/\lambda_h)$ and $N, u, c,$ and H are the Brunt-Vaisala frequency, background neutral wind, horizontal phase velocity of the waves, and density scale height, respectively. The vertical wavelength, λ_z, can be obtained from the vertical wave number, m. Brunt-Vaisala frequency, N, is taken as 0.00872 rad/s ($=2\pi/12$ min), and scale height, H, is taken as 45 km. The horizontal wavelength λ_h and horizontal phase velocity c can be obtained from the airglow measurements. Because there are no measurements of the meridional wind by the CHAMP satellite, the background neutral wind, u, is given as a range from -200 to $+200$ m/s to cover all the possible background wind velocities. The vertical wavelength of gravity wave could be longer than those calculated by using equation (1) at higher altitudes (above the F2 peak) in the thermosphere because dissipation due to viscosity and thermal conductance is not negligible for the dispersion relation of gravity waves, which is the limitation of our assumption.
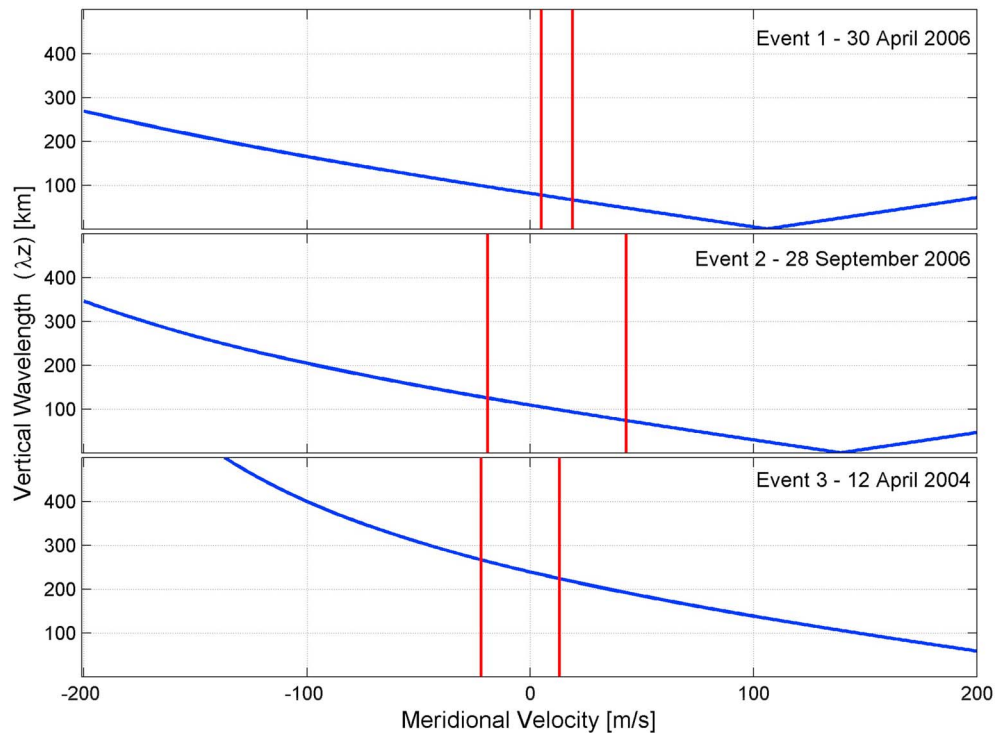
Figure 13. Estimated vertical wavelengths, λ_z, for given northward neutral wind velocities: (a) event 1, (b) event 2, and (c) event 3. Red lines on the figure indicate the range of neutral wind velocities obtained from the HMW07 model during the CHAllenging Minisatellite Payload overpass in the field-of-view of Kototabang.

Figure 13 shows the estimated vertical wavelengths derived from the dispersion relation, λ_z, for the described conditions for all three events. The red lines on Figures 13a–13c indicate the range of background neutral wind velocities obtained from the HWM07 model (Hedin et al., 1988) that are used in the dispersion relation to calculate winds for events 1–3, respectively. A range is given due to different model wind velocities occurring during a CHAMP overpass of the airglow image. For events 1–3, the estimated vertical wavelengths are 60–90, 80–130, and 230–270 km, respectively. According to equation (1), at the altitude of $u = c$, λ_z becomes zero (the critical level) where the gravity wave dissipates. However, the results for all three events do not contain the critical level situation in the model wind data. The altitude of the 630.0-nm airglow emission is considered to be between 200 and 300 km, which makes a thickness of the layer as 100 km. If the vertical wavelength of the wave is much smaller than this thickness of the airglow emission layer, several wave peaks should appear in the layer and compensate each other if we observe it from the ground. The estimated vertical wavelength of gravity waves from the dispersion relationship are comparable or larger than the thickness of the airglow layer. This result is consistent with our conclusion that the observed TIDs in all three cases are caused by gravity waves in the neutral atmosphere.

4. Conclusions

In this study, we have reported the first comparison of ground and satellite measurements of TIDs made by using a 630.0-nm airglow imager and the CHAMP satellite at the equatorial KTB station. During the 7-year period from October 2002 to October 2009, we found only three simultaneous events on 30 April 2006 (event 1), 28 September 2006 (event 2), and 12 April 2004 (event 3). We summarize our observations and conclusions as follows.

1. In all of three events, MSTIDs propagating southward were observed in 630.0-nm airglow images. Horizontal wavelengths of the MSTIDs in the events 1, 2 and 3 were 1,000, 500, and 560 km, respectively. Apparent horizontal velocities of MSTIDs were 112, 124, and 280 m/s for events 1, 2, and 3, respectively. For events 1 and 3, sinusoidal variations of the neutral density were observed at an altitude of 350–400 km with the CHAMP in situ measurements. Horizontal wavelengths of the neutral density variations were 880 and 420 km in the events 1 and 3, respectively. These horizontal wavelengths were consistent with

those observed in the 630.0-nm airglow images. This result indicates that MSTIDs observed in the airglow images were generated by atmospheric gravity waves and that the gravity waves reached at an altitude of 350 and 400 km where the CHAMP satellite flied. On the other hand, in event 2, neutral density variations associated with MSTIDs were not observed at an altitude of 360 km, indicating that gravity waves do not always reach an altitude of 350–400 km.

2. For event 1, both neutral and electron densities observed with the CHAMP satellite show similar wave features. By the CHAMP in situ measurements, plasma density variations associated with MSTIDs were observed only in event 1 and not observed in events 2 and 3. This could be because amplitude of the neutral wind variation is approximately 2% in event 1 and less than 1% in events 2 and 3. Gravity waves with small amplitude of neutral wind variations in events 2 and 3 could not cause discernible plasma density variations.

3. Vertical wavelengths estimated from the phase velocities and periods of the observed MSTIDs according to dispersion relation for atmospheric gravity wave in the three events are 60–270 km. This result is consistent with an idea that gravity waves can exist in the thermosphere and cause the airglow variations observed with the ground-based airglow imager.

Based on these results, we suggest that the observed TIDs of events 1 and 3 are caused by gravity waves in the neutral atmosphere rather than by ionospheric plasma instability. The present result indicates that simultaneous ground and satellite observations are a powerful tool for understanding TIDs in the thermosphere and ionosphere.

References

Bowman, G. G. (1990). A review of some recent work on midlatitude spread-F occurrence as detected by ionosondes. *Journal of Geomagnetism and Geoelectricity*, *42*(2), 109–138.

Fukao, S., Kelley, M. C., Shirakawa, T., Takami, T., Yamamoto, M., Tsuda, T., & Kato, S. (1991). Turbulent upwelling of the mid-latitude ionosphere: 1. Observational results by the MU radar. *Journal of Geophysical Research*, *96*(A3), 3725–3746. https://doi.org/10.1029/90JA02253

Fukushima, D., Shiokawa, K., Otsuka, Y., & Ogawa, T. (2012). Observation of equatorial nighttime medium-scale traveling ionospheric disturbances in 630-nm airglow images over 7 years. *Journal of Geophysical Research*, *117*, A10324. https://doi.org/10.1029/2012JA017758

Hedin, A. E., Spencer, N. W., & Killeen, T. L. (1988). Empirical global model of upper thermosphere winds based on atmosphere and dynamics explorer satellite data. *Journal of Geophysical Research*, *93*, 9959–9978.

Hines, C. O. (1960). Internal atmospheric gravity waves at ionospheric heights. *Canadian Journal of Physics*, *38*, 1441–1481.

Hooke, W. H. (1968). Ionospheric irregularities produced by internal atmospheric gravity waves. *Journal of Atmospheric and Terrestrial Physics*, *30*, 795–823.

Hunsucker, R. D. (1982). Atmospheric gravity waves generated in the high-latitude ionosphere: A review. *Reviews of Geophysics and Space Physics*, *20*, 293–315.

Kotake, N., Otsuka, Y., Ogawa, T., Tsugawa, T., & Saito, A. (2014). Statistical study of medium-scale traveling ionospheric disturbances observed with the GPS networks in southern california. *Earth, Planets and Space*, *59*, 95–102.

Liu, H., Lühr, H., Henize, V., & Kohler, W. (2005). Global distribution of the thermospheric total mass density derived from CHAMP. *Journal of Geophysical Research*, *110*, A04301. https://doi.org/10.1029/2004JA010741

Lühr, H., Park, J., Ritter, P., & Liu, H. (2012). In-situ CHAMP observation of ionosphere-thermosphere coupling. *Space Science Reviews*, *168*, 237–260. https://doi.org/10.1007/s11214-011-9798-4

Mendillo, M., & Baumgardner, J. (1982). Airglow characteristics of equatorial plasma depletions. *Journal of Geophysical Research*, *87*, 7641–7652.

Mendillo, M., Baumgardner, J., Nottingham, D., Aarons, J., Reinisch, B., Scali, J., & Kelley, M. (1997). Investigations of thermospheric-ionospheric dynamics with 6300-Å images from the Arecibo Observatory. *Journal of Geophysical Research*, *102*(A4), 7331–7343. https://doi.org/10.1029/96JA02786

Miller, C. A., Swartz, W. E., Kelley, M. C., Mendillo, M., Nothingham, D., Scali, J., & Reinisch, B. (1997). Electrodynamics of midlatitude spread F: 1. Observations of unstable, gravity wave-induced ionospheric electric fields at tropical latitudes. *Journal of Geophysical Research*, *102*(A6), 11,521–11,532. https://doi.org/10.1029/96JA03839

Müller, S., Luhr, H., & Rentz, S. (2009). Solar and magnetospheric forcing of the low latitude thermospheric mass density as observed by CHAMP. *Annals of Geophysics*, *27*, 2087–2099.

Oberheide, J., Shiokawa, K., Gurubaran, S., Ward, W. E., Fujiwara, H., Kosch, M. J., et al. (2015). The geospace response to variable inputs from the lower atmosphere: A review of the progress made by task group 4 of CAWSES-II. *Progress in Earth and Planetary Science*, *2*, 2. https://doi.org/10.1186/s40645-014-0031-4

Otsuka, Y., Suzuki, K., Nakagawa, S., Nishioka, M., Shiokawa, K., & Tsugawa, T. (2013). GPS observations Of medium-scale traveling ionospheric disturbances over europe. *Annales de Geophysique*, *31*, 163–172. https://doi.org/10.5194/angeo-31-163-2013

Park, J., Luhr, H., Lee, C., Kim, Y. H., Jee, G., & Kim, J.-H. (2014). A climatology of medium-scale gravity wave activity in the midlatitude/low-latitude daytime upper thermosphere as observed by CHAMP. *Journal of Geophysical Research: Space Physics*, *119*, 2187–2196. https://doi.org/10.1002/2013JA019705

Perkins, F. (1973). Spread F and ionospheric currents. *Journal of Geophysical Research*, *78*(1), 218–226. https://doi.org/10.1029/JA078i001p00218

Reigber, C., Balmino, G., Schwintzer, P., Biancale, R., Bode, A., Lemoine, J.-M., et al. (2002). A high-quality global gravity field model from CHAMP GPS tracking data and accelerometry (EIGEN-1S). *Geophysical Research Letters*, *29*(14), 1692. https://doi.org/10.1029/2002GL015064

Shiokawa, K., Otsuka, Y., Ihara, C., Ogawa, T., & Rich, F. J. (2003). Ground and satellite observations of nighttime medium-scale travelling ionospheric disturbance at midlatitude. *Journal of Geophysical Research*, *108*(A4), 1145. https://doi.org/10.1029/2002JA009639

Shiokawa, K., Otsuka, Y., & Ogawa, T. (2006). Quasiperiodic southward moving waves in 630-nm airglow images in the equtorial thermosphere. *Journal of Geophysical Research*, *111*, A06301. https://doi.org/10.1029/2005JA011406

Sobral, J. H. A., Abdu, M. A., & Sahai, Y. (1985). Equatorial plasma bubble eastward velocity characteristics from scanning airglow photometer measurements over Cachoeira Paulista. *Journal of Atmospheric and Terrestrial Physics*, *47*, 895–900.

Torr, M. R., & Torr, D. G. (1982). The role of metastable species in the thermosphere. *Reviews of Geophysics*, *20*, 91–144.

Tsugawa, T., Saito, A., & Otsuka, Y. (2004). A statistical study of large-scale traveling ionospheric disturbances using the GPS network in Japan. *Journal of Geophysical Research*, *109*, A06302. https://doi.org/10.1029/2003JA010302

Vadas, S. L. (2007). Horizontal and vertical propagation and dissipation of gravity waves in the thermosphere from lower atmospheric and thermospheric sources. *Journal of Geophysical Research*, *112*, A06305. https://doi.org/10.1029/2006JA011845

Waldock, J. A., & Jones, T. B. (1986). HF doppler observations of medium-scale traveling ionospheric disturbances at mid-latitudes. *Journal of Atmospheric and Terrestrial Physics*, *48*(3), 245–260. https://doi.org/10.1016/0021-9169(86)90099-1

Yokoyama, T., Hysell, D. L., Otsuka, Y., & Yamamoto, M. (2009). Three-dimensional simulation of the coupled Perkins and Es-layer instabilities in the nighttime midlatitude ionosphere. *Journal of Geophysical Research*, *114*, A03308. https://doi.org/10.1029/2008JA013789